## RESEARCH ARTICLE

Check for updates

# Immobilization of Brønsted basic hexaniobate on the Lewis acidic zirconia using an emulsion assisted self-assembly strategy for synergistic boosting of nerve agent simulant decontamination†

Huifang Liu,[a] Xiangrong Sun,[c] Jing Dong,*[b] Chengpeng Liu,[a] Wei Lu,[a] Zhemi Xu,[b] Ni Zhen,[a] Di Zhang,[a] Yingnan Chi [ID] *[a] and Changwen Hu [ID] [a]

The hydrolytic decontamination of organophosphorus nerve agents can be promoted using Brønsted bases or Lewis acids, but the fabrication of catalytic materials with both Lewis acidic centers and Brønsted base sites is a great challenge due to their essential incompatibility. Herein, a facile and straightforward emulsion assisted self-assembly approach has been developed to immobilize a Brønsted basic hexanio-bate cluster on the Lewis acidic zirconia. The obtained $[C_{16}H_{33}N(CH_3)_3]_6KHNb_6O_{19}/ZrO_2$ ($C_{16}N$-$Nb_6$/$ZrO_2$) exhibits a remarkable catalytic activity for the hydrolysis of a Sarin simulant (DMNP): 100% of DMNP was converted under ambient conditions without using basic additives. Based on the control experiments and spectroscopic analyses, a possible reaction mechanism was proposed, suggesting that such excellent catalytic performance of $C_{16}N$-$Nb_6$/$ZrO_2$ is attributed to the synergistic effect between molecular level accessible Lewis acidic $ZrO_2$ (activating substrate molecules) and Brønsted basic hexaniobates (activating water molecules). As a broad-spectrum catalyst, $C_{16}N$-$Nb_6$/$ZrO_2$ also shows satisfactory performance for the oxidative decontamination of a sulfur mustard simulant.

## Introduction

Organophosphates have historically been used as chemical warfare agents (nerve agents, such as Sarin, Soman and VX) since World War I, and to date, they are still employed as insecticides or used for terrorist purposes. They continue to pose a safety and security threat to both environment and humans as they can cause rapid death by inhibiting signal transmission from the central nervous system to muscles.[1–4] In this regard, there is a compelling need to develop viable strategies to decontaminate organophosphorus nerve agents in a facile and eco-friendly way. Hydrolysis using Brønsted bases

or Lewis acids is a primary way to break the P–X bonds (X = F, CN, *etc.*) in organophosphorus nerve agents.[5] Although basic hydrolysis is effective for Sarin and Soman, the use of stoichiometric strong alkalis makes this route less attractive. Recently, the hydrolysis using Lewis acid catalysts, especially Zr-containing catalysts, has attracted increasing attention.[6–11] Since the strongly Lewis acidic Zr sites are available to bind and activate the P=O bond, the hydrolysis kinetics of organophosphonates is significantly improved.[12–14] The work of G. W. Peterson's group reveals that zirconium hydroxide is a promising candidate for hydrolytic decontamination of Soman and VX.[15] In addition, a series of Zr-based metal–organic frameworks (MOFs) exhibit excellent catalytic activities for the hydrolysis of nerve agents, but their performance highly depends on the use of a basic buffer (*N*-ethylmorpholine, pH = 10).[16–19] Such results imply that the incorporation of Lewis acid catalysts with Brønsted base sites can boost the hydrolytic decontamination of nerve agents.[20,21] Nevertheless, the combination of the Lewis acid catalyst with the Brønsted base site is a great synthetic challenge due to their essential incompatibility.

Polyoxoniobates (PONbs) are a subfamily of polyoxometalates (POMs)[22–24] and both their synthesis chemistry and catalysis chemistry are far behind those of other POM

*[a]Key Laboratory of Cluster Science Ministry of Education, Beijing Key Laboratory of Photoelectronic/Electrophotonic Conversion Materials, School of Chemistry and Chemical Engineering, Beijing Institute of Technology, Beijing, 100081, People's Republic of China. E-mail: chiyingnan7887@bit.edu.cn*
*[b]College of Chemistry and Materials Engineering, Beijing Technology and Business University, 11 Fucheng Road, Beijing, 100048, People's Republic of China. E-mail: 20200808@btbu.edu.cn*
*[c]Jiaxiang Country Branch of Jining Municipal Ecology and Environment Bureau, Jining, 272400, People's Republic of China*
†Electronic supplementary information (ESI) available. See DOI: https://doi.org/10.1039/d2qi02484e

members.[25–31] Recently, the catalytic activities of PONbs in the decontamination of chemical warfare agents and/or their simulants have been explored. Our investigations show that PONbs can promote the oxidative detoxification of sulfur mustard and VX simulants due to their ability to activate hydrogen peroxide.[32–36] In addition, PONbs have basic surface oxygen atoms,[37–39] which can accelerate the hydrolysis of nerve agents.[40,41] Nyman *et al.* initially demonstrated the hydrolysis of Sarin and Soman using homogeneous Lindqvist $[Nb_6O_{19}]^{8-}$.[42] Then, Hill and Zheng reported that Keggin-type PONb, $K_{12}[Ti_2O_2][XNb_{12}O_{40}]$ (X = Ge or Si), and copper-containing PONb, $H_2Li_5Na_5K_5[Cu(en)_2]_7[Nb_{47}O_{128}(OH)_6(CO_3)_2]\cdot20H_2O$ (en = ethylenediamine), as solid bases can catalyze the hydrolysis of nerve agent simulants, but their sluggish hydrolysis kinetics leaves much room for improvement.[43,44] Considering the good catalytic performances of Zr-based catalysts in the hydrolysis reaction, the immobilization of basic PONbs on the Lewis acidic supports would provide an efficient way to realize the rapid decontamination of nerve agents. However, the immobilization of PONbs, which are stable under alkaline conditions with a high negative charge density, is difficult.[33,45,46] To our knowledge, the combination of PONbs with a Lewis acid supporter is rarely explored.

Emulsion assisted self-assembly has been proved to be a facile and straightforward method to prepare functionalized materials, such as polymer particles, graphene oxide and metal oxides.[47–50] In the self-assembly process, an emulsion was formed in the presence of surfactants and the reactions (such as polymerization, hydrolysis, *etc.*) occur at the interface of the emulsion droplets, leading to the materials with a high specific surface area, tunable size and structure, and narrow molecular weight distribution. Recently, a series of amphiphilic POMs were prepared by the electrostatic assembly of polyanions with surfactants, which not only can stabilize an emulsion but also catalyze organic reactions at the liquid/liquid interface.[51–54] However, the emulsion stabilized by surfactant modified POMs was rarely used to prepare POM-based materials. To our knowledge, the only example was reported in Liu's group where a POM modified polystyrene latex particle was prepared by the emulsion assisted assembly using methyl methacrylate functionalized tri-vacant Keggin-type $\{PW_9O_{37}\}$ as a surfactant.[55]

In our previous study, amphiphilic PONbs ($[C_nH_{2n+1}N(CH_3)_3]_7HNb_6O_{19}$, n = 14, 16 and 18) were synthesized by the electrostatic assembly of hexaniobate with quaternary ammoniums with a long alkyl chain, which can catalyze hydrolytic and oxidative detoxification of nerve agent and sulfur mustard simulants in an emulsion system.[35] To advance our research in the design and construction of PONb-based decontamination materials, herein the Brønsted basic hexaniobate was immobilized on the Lewis acidic zirconia by a facile emulsion assisted self-assembly using amphiphilic $[C_{16}H_{33}N(CH_3)_3]_6KHNb_6O_{19}$ ($C_{16}N-Nb_6$) as an emulsifier. As a combination of the Brønsted basic $Nb_6$ with Lewis acidic Zr sites, the synthesized $C_{16}N-Nb_6/ZrO_2$ exhibits remarkable catalytic performance towards the hydrolytic degradation of dimethyl 4-nitrophenyl phosphate (DMNP), a nerve agent simulant, under basic additive-free conditions. Moreover, the synergistic catalytic mechanism was supported by the control experiments and spectroscopic analyses.

## Results and discussion

### Synthesis and characterization of the $C_{16}N-Nb_6/ZrO_2$ composite

The fabrication of the $C_{16}N-Nb_6/ZrO_2$ composite is illustrated in Scheme 1. First, a stable water-in-oil (W/O) type emulsion (Fig. S1†) was formed by vigorously stirring a mixture of water and toluene containing the amphiphilic hexaniobate ($C_{16}N-Nb_6$). Then, zirconium *n*-butoxide (ZB) was dropped slowly into the emulsion and gradually dispersed to the water–oil interface, where $ZrO_2$ was *in situ* generated by hydrolysis and simultaneously assembled with $C_{16}N-Nb_6$ to form the $C_{16}N-Nb_6/ZrO_2$ composite. During the assembly process, the amphiphilic hexaniobate plays dual roles: as a PONb source and an emulsifier. To our knowledge, this is the first example of using an emulsion to prepare PONb-based materials. Compared with the reported methods for preparing POM-based materials,[56–59] the emulsion assisted self-assembly strategy is facile and straightforward. In addition, the control experiments reveal that the $Nb_6$ loading amount can be readily regulated by the mass ratio of $C_{16}N-Nb_6$ to the zirconium *n*-butoxide precursor, and according to inductively coupled plasma atomic emission spectrometry (ICP-AES), five composites with $Nb_6$ loading amounts of 4% (4%-$C_{16}N-Nb_6/ZrO_2$), 6% (6%-$C_{16}N-Nb_6/ZrO_2$), 9% (9%-$C_{16}N-Nb_6/ZrO_2$), 11% (11%-$C_{16}N-Nb_6/ZrO_2$) and 19% (19%-$C_{16}N-Nb_6/ZrO_2$) were obtained (Table S1†), respectively. $C_{16}N-Nb_6/ZrO_2$ with an $Nb_6$ loading amount of 11% was used in the following characterization.

The Fourier transform infrared (FT-IR) spectra of $C_{16}N-Nb_6/ZrO_2$, $C_{16}N-Nb_6$ and $ZrO_2$ are illustrated in Fig. 1a and S2.† $C_{16}N-Nb_6$ displays three characteristic peaks in the region of 500–1000 cm$^{-1}$, attributed to the stretching vibrations of the
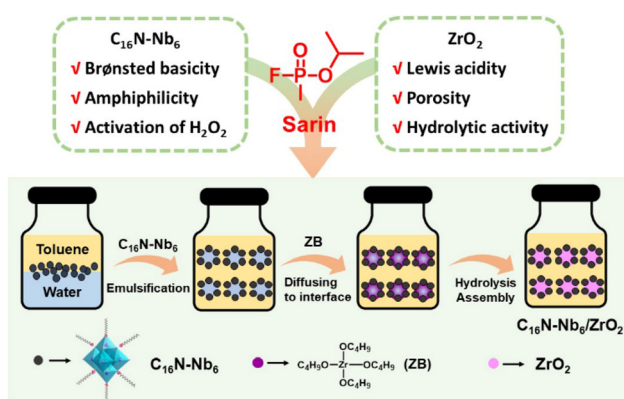


**Scheme 1** Illustration of the design and fabrication of the $C_{16}N-Nb_6/ZrO_2$ composite using an emulsion assisted self-assembly approach.

This journal is © the Partner Organisations 2023

*Inorg. Chem. Front.*, 2023, **10**, 1436–1446 | **1437**

**Fig. 1** (a) The FT-IR spectra of $C_{16}N-Nb_6/ZrO_2$, $C_{16}N-Nb_6$ and $ZrO_2$; (b) $N_2$ adsorption and desorption isotherms of $C_{16}N-Nb_6/ZrO_2$ and $ZrO_2$ measured at 77 K; (c) zeta potential distribution of $C_{16}N-Nb_6/ZrO_2$, $C_{16}N-Nb_6$ and $ZrO_2$ in water; (d) high-resolution Nb 3d XPS spectra of $C_{16}N-Nb_6/ZrO_2$ and $C_{16}N-Nb_6$.

$Nb-O_b-Nb$ (555 and 645 cm$^{-1}$, b: bridge oxygen atoms) and $Nb=O_t$ (879 cm$^{-1}$, t: terminal oxygen atoms) bonds in the hexaniobate cluster. The peaks at 2971 and 2848 cm$^{-1}$ belong to the asymmetric vibration of $CH_2$ in the organic ammonium cation.[35] For $ZrO_2$, the weak peak at 838 cm$^{-1}$ is assigned to the stretching vibration of the Zr–O bond and the broad bands at 1622 and 1331 cm$^{-1}$ are associated with the bending vibration of water molecules.[60] The characteristic peaks of $Nb_6$, cetyltrimethyl ammonium cation and $ZrO_2$ can be observed in the FT-IR spectrum of $C_{16}N-Nb_6/ZrO_2$ (red line in Fig. 1a and S2†), suggesting the successful combination of $C_{16}N-Nb_6$ with $ZrO_2$. The vibrations of $Nb_6$ are rather weak due to its overlap with the strong absorption bands of $ZrO_2$. We speculate that during the assembly process, the organic ammonium cation acts as a protective agent to improve the compatibility of the basic $Nb_6$ cluster with the acidic $ZrO_2$. According to the TG curves of $C_{16}N-Nb_6$ and $C_{16}N-Nb_6/ZrO_2$ (Fig. S3†), in the composite the weight percentages of $C_{16}N-Nb_6$ and $ZrO_2$ are about 49.4 wt% and 50.6 wt%, respectively.

The $N_2$ adsorption and desorption isotherms of $C_{16}N-Nb_6/ZrO_2$ and $ZrO_2$ are presented in Fig. 1b. $C_{16}N-Nb_6/ZrO_2$ shows a type IV isotherm pattern with a hysteresis loop, indicating the presence of mesopores in the composite. The Brunauer–Emmett–Teller (BET) surface area of $C_{16}N-Nb_6/ZrO_2$ is 41.6 m$^2$ g$^{-1}$, which is obviously lower than that of the $ZrO_2$ (242.8 m$^2$ g$^{-1}$, Table S2†). As shown in Fig. 1c, the $ZrO_2$ dispersed in an aqueous medium exhibits a positive charge ($\xi$ = 24.04 mV), probably due to the protonation of the surface O atom.[61,62] After combining with $C_{16}N-Nb_6$ ($\xi$ = −9.76 mV), the zeta potential of $C_{16}N-Nb_6/ZrO_2$ shifts to a lower value ($\xi$ = 2.09 mV). Based on the above results, it can be concluded that the change in the specific surface area and surface potential distribution reveals the successful immobilization of $C_{16}N-Nb_6$ on the $ZrO_2$.

To further confirm the elemental compositions and oxidation states, the X-ray photoelectron spectrum (XPS) of the as-synthesized $C_{16}N-Nb_6/ZrO_2$ was recorded and compared with those of $C_{16}N-Nb_6$ and $ZrO_2$. The survey XPS spectrum in Fig. S3† exhibits the presence of Zr, Nb, C, N and O elements in $C_{16}N-Nb_6/ZrO_2$. The high-resolution XPS Nb 3d spectrum of $C_{16}N-Nb_6/ZrO_2$ displays two peaks at 208.8 eV and 206.0 eV (Fig. 1d), which can be assigned to the Nb $3d_{5/2}$ and Nb $3d_{3/2}$ with a +5 oxidation state, respectively.[33] Compared with that of the $C_{16}N-Nb_6$ precursor (two peaks at 208.5 eV and 205.7 eV correspond to Nb $3d_{5/2}$ and Nb $3d_{3/2}$, respectively), the binding energy of Nb 3d in $C_{16}N-Nb_6/ZrO_2$ shifts to a higher region by about 0.3 eV, demonstrating the strong interaction between $C_{16}N-Nb_6$ and $ZrO_2$ in the $C_{16}N-Nb_6/ZrO_2$ composite.

The morphology of $C_{16}N-Nb_6/ZrO_2$ is investigated by scanning electron microscopy (SEM) and high-resolution transmission electron microscopy (HRTEM). The SEM image of $C_{16}N-Nb_6/ZrO_2$ (Fig. 2a) shows small particles with a diameter of about 20 nm, which is in line with the morphology of the reported $ZrO_2$-based materials.[63,64] No lattice fringe was observed in the HRTEM image (Fig. 2b), demonstrating the amorphous structure of the as-prepared composite. In addition, high-angle annular dark-field scanning transmission electron microscopy (HAADF-STEM) and energy dispersive X-ray (EDX) elemental mapping were carried out to further determine the elemental distribution. As shown in the HAADF-STEM image (Fig. 2c), the heavy atoms (such as Zr and Nb) are brighter than the light atoms (such as O and N). The EDX mapping analysis reveals that niobium, zirconium and nitrogen are evenly dispersed in the $C_{16}N-Nb_6/ZrO_2$ composite (Fig. 2d–f). Moreover, broad diffraction PXRD peaks of $C_{16}N-Nb_6/ZrO_2$ indicate that the as-prepared composite is amorphous (Fig. S4†). There is no characteristic diffraction of $C_{16}N-Nb_6$, further revealing that the hexaniobate clusters are uniformly dispersed in the $C_{16}N-Nb_6/ZrO_2$ composite. This result indicates that the emulsion droplets stabilized by amphiphilic PONb provide a special reaction environment, where $C_{16}N-Nb_6$ assembles with *in situ* formed $ZrO_2$ in a controlled way.



**Fig. 2** (a) SEM image, (b) TEM image, (c) HAADF-STEM image, and (d–f) EDX elemental mappings of the $C_{16}N-Nb_6/ZrO_2$ composite.

In addition, the water contact angles of $C_{16}N\text{-}Nb_6/ZrO_2$, $ZrO_2$, and $C_{16}N\text{-}Nb_6$ were measured. $ZrO_2$ is hydrophilic with a water contact angle of 26° (Fig. S5†). The combination of $ZrO_2$ with $C_{16}N\text{-}Nb_6$ makes the $C_{16}N\text{-}Nb_6/ZrO_2$ composite (with a contact angle of 61°) to have similar surface wettability to that of $C_{16}N\text{-}Nb_6$ (with a contact angle of 64°). Importantly, the enhancement of the surface hydrophobicity would promote the contact of organic substrates (such as DMNP) with the hexaniobate and Zr sites on the composite, thereby accelerating the hydrolytic rate of nerve agents.

### Hydrolytic decontamination of the nerve agent simulant

Given the coexistence of Zr centers (Lewis acid sites) and hexaniobate clusters (Brønsted base sites) in the as-prepared $C_{16}N\text{-}Nb_6/ZrO_2$ composite, the hydrolysis of DMNP, a nerve agent simulant, was selected to evaluate its catalytic activity. Before the decontamination study, we tested the acid and base sites of the composite. The surface basicity was first investigated using phenolphthalein as an indicator. As shown in the Fig. 3a inset, a colour change from pale to light pink was observed when phenolphthalein was dropped into the slurry containing $C_{16}N\text{-}Nb_6/ZrO_2$, while the colour of the $ZrO_2$ slurry remains unchanged. This phenomenon reveals that the introduction of $C_{16}N\text{-}Nb_6$ endows the material with Brønsted basicity. To measure the basic site distribution and the basicity capacity of the composite, temperature-programmed desorption of $CO_2$ ($CO_2$-TPD) was conducted. A comparison of the $CO_2$-TPD profiles of $C_{16}N\text{-}Nb_6/ZrO_2$ and $ZrO_2$ is shown in Fig. 3a, $C_{16}N\text{-}Nb_6/ZrO_2$ has the maximum $CO_2$ desorption at 126 °C (corresponding to the weak base sites), while $ZrO_2$ reaches the desorption peak at 106 °C. The total basicity capacity of $C_{16}N\text{-}Nb_6/ZrO_2$ and $ZrO_2$ was calculated to be 13.5 and 0.92 mmol $g^{-1}$, respectively. These results verify that the immobilization of hexaniobate on the $ZrO_2$ renders the composite with Brønsted base sites. In addition, temperature-programmed desorption of ammonia ($NH_3$-TPD) measurement was performed to detect the Lewis acid sites. As shown in Fig. 3b, the broad desorption peaks at about 148 °C were observed in both the $NH_3$-TPD profiles of $C_{16}N\text{-}Nb_6/ZrO_2$ and $ZrO_2$, suggesting the presence of weak acid sites.[65,66] The density of the Lewis acid sites on $C_{16}N\text{-}Nb_6/ZrO_2$ was calculated to be 121 mmol $g^{-1}$, which is slightly lower than that of $ZrO_2$ (133 mmol $g^{-1}$). The coexistence of Lewis acid sites and

Brønsted base sites makes the $C_{16}N\text{-}Nb_6/ZrO_2$ composite a promising catalyst for the hydrolytic decontamination of nerve agents.

In a typical reaction, the $C_{16}N\text{-}Nb_6/ZrO_2$ composite was dispersed in a mixture solution of $H_2O$ and $CD_3CN$ (volume ratio 3 : 2) with an initial pH value of about 9.3 and DMNP was injected to start the hydrolytic reaction. The decontamination process was performed under ambient conditions without using any basic co-catalysts and the reaction progress was monitored by $^{31}P$ NMR spectroscopy at various time intervals. As shown in Fig. 4b, the $^{31}P$ NMR spectral measurements reveal a gradual disappearance of DMNP ($\delta = -4.8$ ppm) and an increase of the peak at $\delta = 2.6$ ppm, attributed to the hydrolysis product, dimethyl phosphate (DMP). Moreover, no toxic byproduct was detected during the hydrolysis (Fig. 4b and S7†). As shown in Fig. 4c, DMNP was completely consumed within 6 h under basic additive-free conditions and the half-life of DMNP is about 30 min. In contrast, a negligible amount of DMNP was converted in the blank experiment without a catalyst (Fig. 5). To our knowledge, the catalytic performance of the $C_{16}N\text{-}Nb_6/ZrO_2$ composite in the present work outperforms those of most of the reported catalytic materials, such as POMs,[26,43,44,67,68] MOFs[69] and oxides/hydroxides[70] (Table S3†).

To further investigate the influence of Lewis acid sites and Brønsted base sites on the catalytic hydrolysis reaction, the following control experiments were conducted. When $ZrO_2$ was used, only a trace amount of DMNP was converted under the standard decontamination conditions (Table 1, entry 6 and Fig. 5). The amphiphilic $C_{16}N\text{-}Nb_6$ also gives a negligible conversion (<5%) (Table 1, entry 7 and Fig. 5). The above results indicate that neither the Lewis acidic $ZrO_2$ nor the Brønsted basic $C_{16}N\text{-}Nb_6$ alone can effectively accelerate the decontamination reaction, implying the interesting synergistic effect between the two components. Although the conversion of DMNP can be increased to 27% using a physical mixture of $ZrO_2$ and $C_{16}N\text{-}Nb_6$ (Fig. 5), its catalytic activity is still much
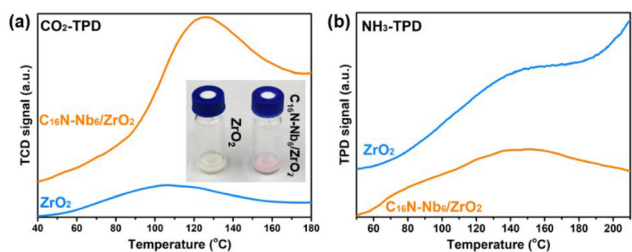
**Fig. 3** (a) $CO_2$-TPD of $C_{16}N\text{-}Nb_6/ZrO_2$ and $ZrO_2$, inset: optical photographs of $C_{16}N\text{-}Nb_6/ZrO_2$ and $ZrO_2$ slurry after adding phenolphthalein. (b) $NH_3$-TPD of $C_{16}N\text{-}Nb_6/ZrO_2$ and $ZrO_2$.
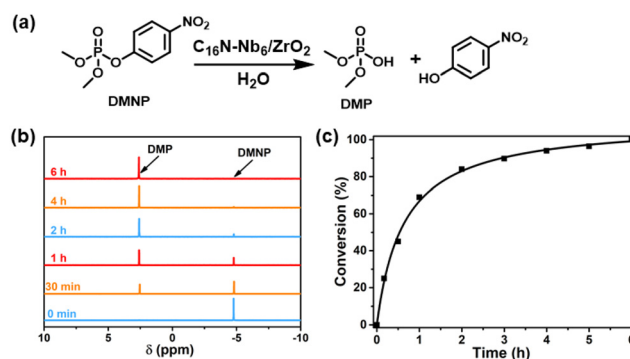
**Fig. 4** (a) Catalytic hydrolysis reaction of the phosphonate-based nerve agent simulant DMNP using $C_{16}N\text{-}Nb_6/ZrO_2$; (b) $^{31}P$ NMR of DMNP hydrolysis catalyzed by $C_{16}N\text{-}Nb_6/ZrO_2$ at various intervals of time; (c) time profile for DMNP degradation. Reaction conditions: DMNP (5 mg), $H_2O$ (300 μL), $CD_3CN$ (200 μL), $C_{16}N\text{-}Nb_6/ZrO_2$ (15 mg), and room temperature for 6 h.

This journal is © the Partner Organisations 2023

*Inorg. Chem. Front.*, 2023, **10**, 1436–1446 | **1439**

**Fig. 5** Catalytic hydrolysis of DMNP with different catalysts without using any basic co-catalysts. Reaction conditions: DMNP (5 mg), H$_2$O (300 μL), CD$_3$CN (200 μL), catalyst, and room temperature for 6 h.
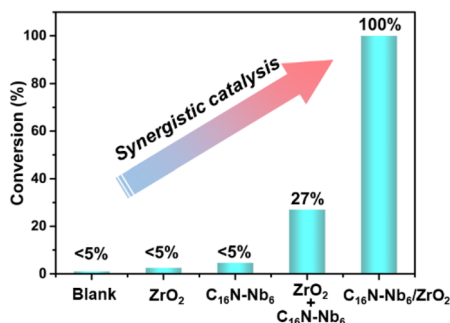
**Table 1** Hydrolytic degradation of DMNP using various catalysts[a]

| Entry | Catalyst | Conditions | Conv. (%) |
|---|---|---|---|
| 1 | 19%-C$_{16}$-Nb$_6$/ZrO$_2$ | 15 mg | 100 |
| 2 | 11%-C$_{16}$-Nb$_6$/ZrO$_2$ | 15 mg | 100 |
| 3 | 9%-C$_{16}$-Nb$_6$/ZrO$_2$ | 15 mg | 97 |
| 4 | 6%-C$_{16}$-Nb$_6$/ZrO$_2$ | 15 mg | 88 |
| 5 | 4%-C$_{16}$-Nb$_6$/ZrO$_2$ | 15 mg | 83 |
| 6 | ZrO$_2$ | 13.3 mg | Trace |
| 7 | C$_{16}$N-Nb$_6$ | 1.7 mg | Trace |
| 8[b] | ZrO$_2$ + NaOH | 13.3 mg, pH = 9.3 | 29 |

[a] Reaction conditions: DMNP (5 mg), H$_2$O (300 μL), CD$_3$CN (200 μL), catalyst, and room temperature for 6 h. All the hydrolysis of DMNP was performed in a heterogeneous system. [b] NaOH was added to the reaction mixture to adjust the pH value.

lower than that of the as-prepared C$_{16}$N-Nb$_6$/ZrO$_2$ composite (100%). We speculate that the molecular level accessible Lewis acidic sites and Brønsted basic sites play a key role in the rapid hydrolysis of DMNP. In addition, the catalytic performance of C$_{16}$N-Nb$_6$/ZrO$_2$ is affected by the content of Nb$_6$, the conversion of DMNP increased from 83% to 100% with the loading amount of Nb$_6$ being improved from 4% to 11% (Table 1, entries 1–5), and the C$_{16}$N-Nb$_6$/ZrO$_2$ with 11% Nb$_6$ loading was used in the following experiments.

To understand the catalytic role of C$_{16}$N-Nb$_6$/ZrO$_2$ in the hydrolysis reaction, the composite was treated with DMNP for 1 h in a non-aqueous system and the XPS measurement was performed on the isolated sample. As shown in Fig. 6a, after
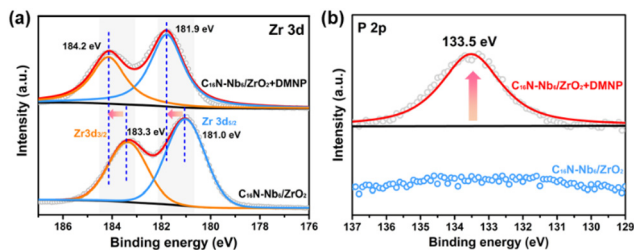
treating with DMNP, the high-resolution Zr 3d spectrum of C$_{16}$N-Nb$_6$/ZrO$_2$ exhibits an obvious binding energy shift from 183.3 to 184.2 eV for Zr 3d$_{3/2}$ and from 181.0 to 181.9 eV for Zr 3d$_{5/2}$, respectively. The obvious increase of the Zr 3d binding energy (0.9 eV) implies the strong interaction of Zr sites with the substrate, which is consistent with previous reports.[71] Furthermore, a new peak at 133.5 eV appeared in the high-resolution P 2p XPS spectrum of DMNP-treated C$_{16}$N-Nb$_6$/ZrO$_2$ (Fig. 6b), which is assigned to P=O of the surface-bound phosphate species.[71] The above results demonstrate that the Lewis acidic Zr sites in the composite can bind and activate the P=O bond of DMNP during the catalytic reaction. The role of solid base Nb$_6$ was also investigated. As the initial pH value of the reaction solution was 9.3 in the presence of C$_{16}$N-Nb$_6$/ZrO$_2$, we first think that the role of basic C$_{16}$N-Nb$_6$ is to generate OH$^-$ to attack the P center of the substrate. Then, the control experiment using ZrO$_2$ with a pH of 9.3 adjusted using NaOH was performed, which only converted 29% of DMNP (Table 1, entry 8 and Fig. S8†). This result implies that the main role of hexaniobate is not to accept the proton of water to release OH$^-$, but to activate water molecules by its basic surface oxygen atoms.

Based on the previous hydrolysis studies in the Zr-containing catalytic system and the above experimental data, we proposed a possible mechanism for the catalytic decontamination of DMNP by C$_{16}$N-Nb$_6$/ZrO$_2$ (Fig. 7). First, the Lewis acidic Zr centers coordinate with the phosphoryl oxygen of DMNP, activating the P=O bond. Meanwhile, water molecules interact with the bridging oxygen atoms of the Lindqvist hexaniobate cluster to form intermediate A. Subsequently, the oxygen atom of the activated water molecule attacks the P center of adjacent DMNP giving intermediate B with a pentacoordinated P center and a protonated hexaniobate. Then, the elimination of nitrophenoxide consumes the proton on the hexaniobate cluster, leaving the intermediate C (DMP binds to the Zr sites). Finally, the bonded product dissociates to the reaction solution regenerating the C$_{16}$N-Nb$_6$/ZrO$_2$ catalyst.



**Fig. 6** High-resolution XPS spectra of the C$_{16}$N-Nb$_6$/ZrO$_2$ composite treated with DMNP in a non-aqueous system: (a) Zr 3d and (b) P 2p.
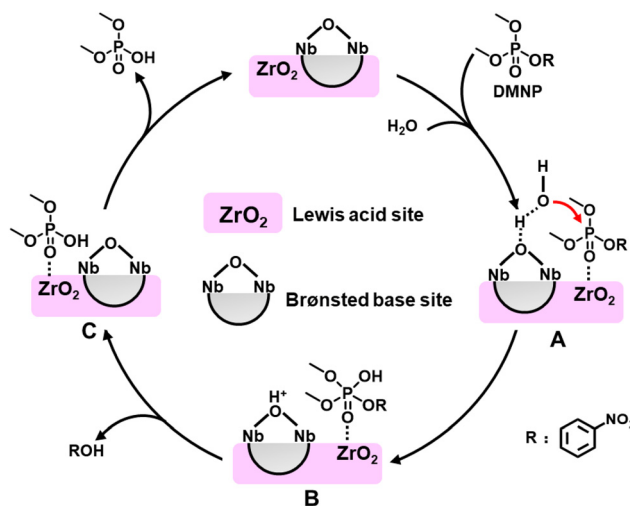


**Fig. 7** The possible hydrolytic degradation mechanism for DMNP on the C$_{16}$N-Nb$_6$/ZrO$_2$ catalyst.

**1440** | *Inorg. Chem. Front.*, 2023, **10**, 1436–1446

This journal is © the Partner Organisations 2023

The heterogeneous nature of the $C_{16}N$-$Nb_6$/$ZrO_2$ catalyst was evaluated using the leaching test. After the hydrolysis was performed for 1 h with a conversion of about 70%, the solid catalyst was filtered off from the reaction mixture and the resulting solution continued to react under the otherwise identical conditions. The negligible conversion was observed for another 5 h (Fig. 8a), suggesting that the hexaniobate is stably immobilized on $ZrO_2$. Then, we investigated the long-term stability of the $C_{16}N$-$Nb_6$/$ZrO_2$. After the first run, the solid catalyst was filtered from the reaction system and used for the next run after washing. Unfortunately, a decrease in DMNP conversion (about 20%) was observed for the first three cycles (Fig. 8b). Based on the literature research,[20,21] we speculate that the decrease in the catalytic performance is probably related to the adsorption of the acidic product (DMP) on the catalytic active sites. This point was proved by the following control experiments and spectroscopic analysis. First, an obvious decrease in the catalytic activity of $C_{16}N$-$Nb_6$/$ZrO_2$ (the conversion of DMNP decreases from 100% to 69%) was observed upon the addition of extra DMP to the standard catalytic reaction. Moreover, after the third run, the isolated catalyst was washed with acetonitrile thoroughly and measured by FT-IR spectroscopy. As shown in Fig. S9,† the characteristic peaks of hexaniobate and $ZrO_2$ were maintained, but new peaks at 1164 cm$^{-1}$ and 1110 cm$^{-1}$ assigned to the $\nu_a$(O–P–O) and $\nu_s$(O–P–O),[71] respectively, were detected. The isolated sample was further characterized by XPS. After three cycles, the peaks of Zr $3d_{3/2}$ and Zr $3d_{5/2}$ shift to a higher binding energy (Fig. 8c) and a similar trend is observed in the Nb 3d XPS spectra (Fig. 8d), which indicates the interaction of the Zr center and hexaniobate with the acid hydrolysis product (DMP). To gain a better recycle performance, after three cycles

the $C_{16}N$-$Nb_6$/$ZrO_2$ composite was activated by soaking in KOH solution (1 M) and the catalytic activity of $C_{16}N$-$Nb_6$/$ZrO_2$ was basically recovered after regeneration with 92% and 90% of DMNP conversion in the fourth and fifth runs, respectively (Fig. 8b).

## Oxidative decontamination of the sulfur mustard simulant

Our previous works indicate that PONbs are active in the oxidative decontamination of the sulfur mustard simulant 2-chloroethyl ethyl sulfide (CEES) in the presence of dilute aqueous $H_2O_2$ (3 wt%).[32–36] To explore the broad-spectrum decontamination activity of the as-prepared $C_{16}N$-$Nb_6$/$ZrO_2$ composite, oxidative degradation of CEES was selected as the second model reaction (Fig. 9a). Under the optimized conditions, 93% of the toxic substrate was consumed after 2 h and 83% of selectivity for the less-toxic product, 2-chloroethyl ethyl sulfoxide (CEESO), was observed using $C_{16}N$-$Nb_6$/$ZrO_2$ as the catalyst (Fig. 9b and S10, S11†). In contrast, the test without the catalyst (blank test) shows a negligible CEES removal (Conv. 7%).

To evaluate the contribution of $ZrO_2$ and the hexaniobate cluster to the oxidative process, control experiments with different catalysts were conducted. As shown in Fig. 9c, $C_{16}N$-$Nb_6$ converted 86% of CEES, and a satisfactory selectivity of 96% towards the less toxic CEESO was obtained, while $ZrO_2$ can also interact with $H_2O_2$ to form the Zr-peroxo species (Fig. S12†), showing a moderate catalytic performance (Conv. 47%, Sele. 53%). Furthermore, the catalytic activities of the $C_{16}N$-$Nb_6$/$ZrO_2$ composites with various $C_{16}N$-$Nb_6$ loadings were tested. A significant improvement in the conversion (from 60% to 94%) was obtained by increasing the loading of $Nb_6$ from 4% to 9%, but a further increase in $Nb_6$ loading did not lead to enhanced performance. Based on the above results, we can conclude that the $Nb_6$ cluster is the main activity center towards the selective oxidation of CEES. In addition, the comparison of FT-IR spectra (Fig. S13†) of the catalyst before and after the oxidative decontamination reaction indicates that the structure of $C_{16}N$-$Nb_6$/$ZrO_2$ remains stable under the turnover conditions.
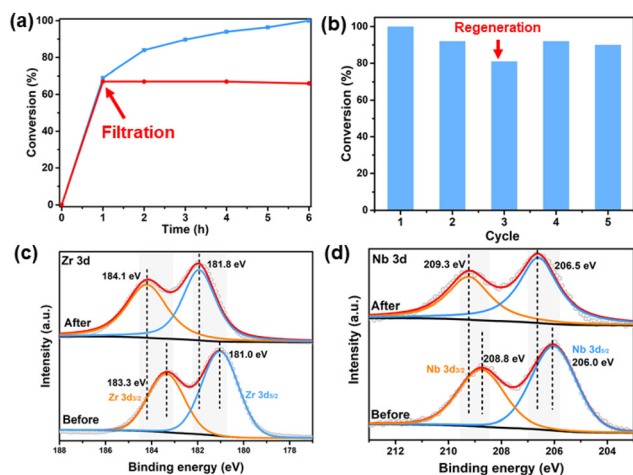


**Fig. 8** (a) Leaching experiment for the hydrolysis of DMNP over $C_{16}N$-$Nb_6$/$ZrO_2$; (b) recycle test for the decontamination reaction using $C_{16}N$-$Nb_6$/$ZrO_2$ as the catalyst. Reaction conditions: DMNP (5 mg), $H_2O$ (300 μL), $CD_3CN$ (200 μL), $C_{16}N$-$Nb_6$/$ZrO_2$ (15 mg), and room temperature for 6 h; (c) high-resolution Zr 3d XPS spectra of $C_{16}N$-$Nb_6$/$ZrO_2$ before and after the catalytic reaction; and (d) high-resolution Nb 3d XPS spectra of $C_{16}N$-$Nb_6$/$ZrO_2$ before and after the catalytic reaction.
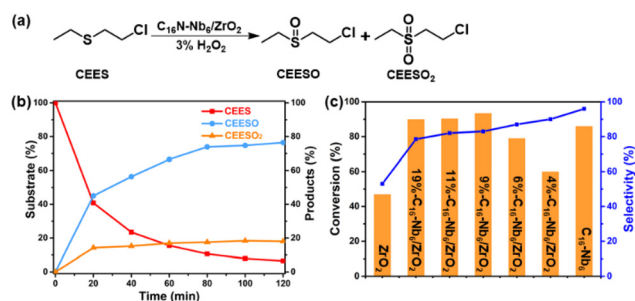


**Fig. 9** (a) Catalytic oxidation degradation of the sulfur mustard simulant CEES by $C_{16}N$-$Nb_6$/$ZrO_2$; (b) concentration profiles of CEES, CEESO, and $CEESO_2$ (2-chloroethyl ethyl sulfone) *versus* reaction time over $C_{16}N$-$Nb_6$/$ZrO_2$; reaction conditions: CEES (0.4 mmol), 1,3-dichlorobenzene (0.2 mmol), $C_{16}N$-$Nb_6$/$ZrO_2$ (10 mg), and aqueous $H_2O_2$ (3 wt%, 0.44 mmol) at room temperature for 2 h. (c) Oxidative decontamination of CEES over different catalysts.

This journal is © the Partner Organisations 2023

*Inorg. Chem. Front.*, 2023, **10**, 1436–1446 | **1441**

## Conclusions

In this report, a catalytic decontamination material containing both Brønsted basic hexaniobate and the Lewis acidic Zr sites has been successfully prepared using a facile emulsion-assisted self-assembly strategy. The obtained $C_{16}N$-$Nb_6$/$ZrO_2$ composite shows remarkable catalytic performance towards the hydrolytic degradation of an organophosphorus nerve agent simulant, DMNP, while $C_{16}N$-$Nb_6$ or $ZrO_2$ alone shows negligible activity. The in-depth mechanism study indicates that the synergistic effect between $C_{16}N$-$Nb_6$ and $ZrO_2$ is of great importance to boost the hydrolytic kinetics. Moreover, the $C_{16}N$-$Nb_6$/$ZrO_2$ composite also shows catalytic activity in the oxidative decontamination of the sulfur mustard simulant. The reported investigation not only provides a highly effective catalyst for the decontamination of chemical warfare agent simulants but also opens up new prospects for the design and fabrication of PONb-based catalytic materials. The combination of surfactant modified PONbs with other functionalized supports is under investigation in our lab.

## Experimental section

### Materials and methods

All the starting chemicals and solvents were of reagent grade, purchased from commercial sources, and used without further purification. **CAUTION**: The simulants of CWAs, DMNP and CEES, are highly toxic and must be handled only by trained personnel using applicable safety procedures in a closed system or a hood under good ventilation.

The XRD patterns were obtained on a Shimadzu XRD-6000 instrument with graphite-monochromatized Cu Kα ($\lambda$ = 1.5406 Å). The XPS analysis was conducted on a PHI VersaProbe III spectrometer using an Al Kα radiation as the X-ray source. The FT-IR spectra were recorded on a JASCO 6300D instrument in the region of 400–4000 $cm^{-1}$. The Brunauer–Emmett–Teller (BET) specific surface areas were measured at 77 K with a Micromeritics ASAP 2000 instrument, and the pore size distributions were estimated using the Barrett–Joyner–Halenda (BJH) method. Elemental analysis (C, H and N) was performed on an ElementarVario EL cube Elmer CHN elemental analyzer and ICP-MS was performed on a ThermoiCAP 6000 atomic emission spectrometer. SEM (JOEL JSE-7500F), TEM (JEOL JEM-2010) and field emission transmission electron microscopy (FEI Talos F200X) were used to observe the morphology and microstructure of the samples. The acidic and basic sites of the synthesized material were measured by $NH_3$-TPD and $CO_2$-TPD, respectively, with a PCA-1200 instrument. The gas chromatographic (GC) analyses were performed on a Shimadzu GC-2014C equipped with an FID detector and an HP-5 ms capillary column. The GC-MS spectra of the products were obtained using an Agilent 7890A-5975C instrument. The $^{31}P$ NMR spectra were recorded on a Bruker 400 MHz instrument in $CD_3CN$, and all the chemical shifts were referenced to an aqueous $H_3PO_4$ solution (85%).

### Preparation of $C_{16}N$-$Nb_6$/$ZrO_2$

The $C_{16}N$-$Nb_6$/$ZrO_2$ composite was prepared using an emulsion assisted self-assembly method. First, a certain amount of $[C_{16}H_{33}N(CH_3)_3]_4K_3HNb_6O_{19}$ ($C_{16}N$-$Nb_6$)[32] was dispersed in toluene (10 mL) and treated with ultrasound for about 5 min. Then, deionized water (20 mL) was added to the above toluene solution and the mixture was strongly shocked and stirred until a stable emulsion was obtained. A toluene solution (1 mL) containing zirconium *n*-butoxide was dropped slowly into the above emulsion system (in an ice-bath) and the reaction mixture was stirred for another 6 h. The final white precipitate, $C_{16}N$-$Nb_6$/$ZrO_2$, was filtered from the reaction mixture, washed with ethanol several times, and dried under vacuum. Various $C_{16}N$-$Nb_6$/$ZrO_2$ composites with different $Nb_6$ loading amounts were obtained by controlling the ratio of zirconium *n*-butoxide to $C_{16}N$-$Nb_6$: 0.3 g of $C_{16}N$-$Nb_6$ and 0.5 g of zirconium *n*-butoxide for $C_{16}N$-$Nb_6$/$ZrO_2$-19%, 0.2 g of $C_{16}N$-$Nb_6$ and 0.6 g of zirconium *n*-butoxide for $C_{16}N$-$Nb_6$/$ZrO_2$-11%, 0.1 g of $C_{16}N$-$Nb_6$ and 0.4 g of zirconium *n*-butoxide for $C_{16}N$-$Nb_6$/$ZrO_2$-9%, 0.1 g of $C_{16}N$-$Nb_6$ and 0.6 g of zirconium *n*-butoxide for $C_{16}N$-$Nb_6$/$ZrO_2$-6%, and 0.1 g of $C_{16}N$-$Nb_6$ and 0.8 g of zirconium *n*-butoxide for $C_{16}N$-$Nb_6$/$ZrO_2$-4%.

### Catalytic hydrolysis of DMNP using $C_{16}N$-$Nb_6$/$ZrO_2$

The as-prepared $C_{16}N$-$Nb_6$/$ZrO_2$ catalyst (15 mg) was added to a mixture solution of $CD_3CN$ (0.2 mL) and water (0.3 mL) and stirred for 5 min to disperse homogeneously. Then, DMNP (100 mg $mL^{-1}$ in $CH_3CN$, 50 µL) was injected to start the decontamination process. The catalytic hydrolysis reaction was performed with stirring at room temperature and the hydrolysis profiles were recorded by $^{31}P$ NMR measurements at various intervals of time. The conversion of DMNP was calculated depending on the peak area ratio of the detected DMNP to DMNP adding the products.

### Catalytic oxidation of CEES using $C_{16}N$-$Nb_6$/$ZrO_2$

The as-prepared $C_{16}N$-$Nb_6$/$ZrO_2$ catalyst (10 mg) was dispersed in $CH_3CN$ (3 mL) and to this solution CEES (0.4 mmol) and 1,3-dichlorobenzene (0.2 mmol, internal standard) were added. After stirring for 5 min, aqueous $H_2O_2$ (3 wt%, 0.44 mmol) was dropped to initiate the decontamination reaction. The products were qualitatively analyzed by GC-MS and the oxidation profiles were monitored using GC.

### Procedure for $NH_3$-TPD and $CO_2$-TPD measurements

$NH_3$-TPD measurements were performed to gain the density distribution and strength of acid sites in $C_{16}N$-$Nb_6$/$ZrO_2$. First, $C_{16}N$-$Nb_6$/$ZrO_2$ (25 mg) was pretreated at 150 °C for 120 min under an Ar blow at a flow rate of 30 mL $min^{-1}$. Then, the sample was exposed to ammonia at 100 °C until saturation and purged under an Ar flow for 30 min to remove the physically adsorbed ammonia before cooling to room temperature. The sample was heated from 40 to 400 °C at a ramping rate of 10 °C $min^{-1}$ under an Ar atmosphere, and ammonia was detected using a thermal conductivity detector.

**1442** | *Inorg. Chem. Front.*, 2023, **10**, 1436–1446

This journal is © the Partner Organisations 2023

$CO_2$-TPD measurements were performed to gain the density distribution and strength of base sites in $C_{16}N$-$Nb_6/ZrO_2$. The procedure for $CO_2$-TPD measurements was similar to that of $NH_3$-TPD, except that He gas was used instead of Ar gas and the adsorption temperature of $CO_2$ was 80 °C.

### Treatment of $C_{16}N$-$Nb_6/ZrO_2$ with DMNP

$C_{16}N$-$Nb_6/ZrO_2$ was dispersed in the anhydrous $CH_3CN$ solution of DMNP and consecutively stirred for 1 h at room temperature. Then, the solid was separated by filtration, washed and characterized by XPS.

## Author contributions

H. F. Liu synthesized and characterized the $C_{16}N$-$Nb_6/ZrO_2$ composite catalyst and J. Dong performed the catalytic hydrolysis of DMNP as well as the oxidation of CEES. X. R. Sun and C. P. Liu helped with data analysis and graphic design. Y. N. Chi and C. W. Hu conceived and directed the research. W. Lu, Z. M. Xu, N. Zhen and D. Zhang gave some advice about the preparation of catalysts and the catalytic experiments.

## Conflicts of interest

There are no conflicts to declare.

## Acknowledgements

## Notes and references

1 J. B. DeCoste and G. W. Peterson, Metal-Organic Frameworks for Air Purification of Toxic Chemicals, *Chem. Rev.*, 2014, **114**, 5695–5727.

2 N. S. Bobbitt, M. L. Mendonca, A. J. Howarth, T. Islamoglu, J. T. Hupp, O. K. Farha and R. Q. Snurr, Metal-Organic Frameworks for the Removal of Toxic Industrial Chemicals and Chemical Warfare Agents, *Chem. Soc. Rev.*, 2017, **46**, 3357–3385.

3 Y. C. Yang, J. A. Baker and J. R. Ward, Decontamination of Chemical Warfare Agents, *Chem. Rev.*, 1992, **92**, 1729–1743.

4 B. M. Smith, Catalytic Methods for the Destruction of Chemical Warfare Agents under Ambient Conditions, *Chem. Soc. Rev.*, 2008, **37**, 470–478.

5 K. Kim, O. G. Tsay, D. A. Atwood and D. G. Churchill, Destruction and Detection of Chemical Warfare Agents, *Chem. Rev.*, 2011, **111**, 5345–5403.

6 K. Vellingiri, L. Philip and K. Kim, Metal-Organic Frameworks as Media for the Catalytic Degradation of Chemical Warfare Agents, *Coord. Chem. Rev.*, 2017, **353**, 159–179.

7 Y. Y. Liu, A. J. Howarth, N. A. Vermeulen, S. Y. Moon, J. T. Hupp and O. K. Farha, Catalytic Degradation of Chemical Warfare Agents and their Simulants by Metal-Organic Frameworks, *Coord. Chem. Rev.*, 2017, **346**, 101–111.

8 R. B. Balow, J. G. Lundin, G. C. Daniels, W. O. Gordon, M. McEntee, G. W. Peterson, J. H. Wynne and P. E. Pehrsson, Environmental Effects on Zirconium Hydroxide Nanoparticles and Chemical Warfare Agent Decomposition: Implications of Atmospheric Water and Carbon Dioxide, *ACS Appl. Mater. Interfaces*, 2017, **9**, 39747–39757.

9 J. Colón-Ortiz, J. M. Landers, W. O. Gordon, A. Balboa, C. J. Karwacki and A. V. Neimark, Disordered Mesoporous Zirconium (Hydr)oxides for Decomposition of Dimethyl Chlorophosphate, *ACS Appl. Mater. Interfaces*, 2019, **11**, 17931–17939.

10 S. Jeon, I. V. Schweigert, P. E. Pehrsson and R. B. Balow, Kinetics of Dimethyl Methylphosphonate Adsorption and Decomposition on Zirconium Hydroxide Using Variable Temperature in Situ Attenuated Total Reflection Infrared Spectroscopy, *ACS Appl. Mater. Interfaces*, 2020, **12**, 14662–14671.

11 J. W. Long, C. N. Chervin, R. B. Balow, S. Jeon, J. B. Miller, M. E. Helms, J. C. Owrutsky, D. R. Rolison and K. P. Fears, Zirconia-based Aerogels for Sorption and Degradation of Dimethyl Methylphosphonate, *Ind. Eng. Chem. Res.*, 2020, **59**, 19584–19592.

12 J. E. Mondloch, M. J. Katz, W. C. Isley III, P. Ghosh, P. L. Liao, W. Bury, G. W. Wagner, M. G. Hall, J. B. DeCoste, G. W. Peterson, R. Q. Snurr, C. J. Cramer, J. T. Hupp and O. K. Farha, Destruction of Chemical Warfare Agents using Metal-Organic Frameworks, *Nat. Mater.*, 2015, **14**, 512–516.

13 M. J. Katz, S. Y. Moon, J. E. Mondloch, M. H. Beyzavi, C. J. Stephenson, J. T. Hupp and O. K. Farha, Exploiting Parameter Space in MOFs: A 20-fold Enhancement of Phosphate-Ester Hydrolysis with UiO-66-$NH_2$, *Chem. Sci.*, 2015, **6**, 2286–2291.

14 K. K. Ma, T. Islamoglu, Z. J. Chen, P. Li, M. C. Wasson, Y. W. Chen, Y. F. Wang, G. W. Peterson, J. H. Xin and O. K. Farha, Scalable and Template-Free Aqueous Synthesis of Zirconium-Based Metal-Organic Framework Coating on Textile Fiber, *J. Am. Chem. Soc.*, 2019, **141**, 15626–15633.

15 T. J. Bandosz, M. Laskoski, J. Mahle, G. Mogilevsky, G. W. Peterson, J. A. Rossin and G. W. Wagner, Reactions of VX, GD, and HD with $Zr(OH)_4$: Near Instantaneous Decontamination of VX, *J. Phys. Chem. C*, 2012, **116**, 11606–11614.

16 S. Y. Moon, Y. Y. Liu, J. T. Hupp and O. K. Farha, Instantaneous Hydrolysis of Nerve-Agent Simulants with a Six-Connected Zirconium-Based Metal-Organic Framework, *Angew. Chem., Int. Ed.*, 2015, **54**, 6795–6799.

17 T. Islamoglu, M. A. Ortuño, E. Proussaloglou, A. J. Howarth, N. A. Vermeulen, A. Atilgan, A. M. Asiri,

This journal is © the Partner Organisations 2023

*Inorg. Chem. Front.*, 2023, **10**, 1436–1446 | **1443**

C. J. Cramer and O. K. Farha, Presence versus Proximity: The Role of Pendant Amines in the Catalytic Hydrolysis of a Nerve Agent Simulant, *Angew. Chem., Int. Ed.*, 2018, **57**, 1949–1953.

18 S. Y. Moon, E. Proussaloglou, G. W. Peterson, J. B. DeCoste, M. G. Hall, A. J. Howarth, J. T. Hupp and O. K. Farha, Detoxification of Chemical Warfare Agents Using a $Zr_6$-Based Metal-Organic Framework/Polymer Mixture, *Chem. – Eur. J.*, 2016, **22**, 14864–14868.

19 Y. Y. Liu, S. Y. Moon, J. T. Hupp and O. K. Farha, Dual-Function Metal Organic Framework as a Versatile Catalyst for Detoxifying Chemical Warfare Agent Simulants, *ACS Nano*, 2015, **9**, 12358–12364.

20 E. López-Maya, C. Montoro, L. M. Rodríguez-Albelo, S. D. A. Cervantes, A. A. Lozano-Pérez, J. L. Cenís, E. Barea and J. A. R. Navarro, Textile/Metal-Organic-Framework Composites as Self-Detoxifying Filters for Chemical-Warfare Agents, *Angew. Chem., Int. Ed.*, 2015, **54**, 6790–6794.

21 R. Gil-San-Millan, E. López-Maya, M. Hall, N. M. Padial, G. W. Peterson, J. B. DeCoste, L. M. Rodríguez-Albelo, J. E. Oltra, E. Barea and J. A. R. Navarro, Chemical Warfare Agents Detoxification Properties of Zirconium Metal-Organic Frameworks by Synergistic Incorporation of Nucleophilic and Basic Sites, *ACS Appl. Mater. Interfaces*, 2017, **9**, 23967–23973.

22 H. Y. Zhao, Y. Z. Li, J. W. Zhao, L. Wang and G. Y. Yang, State-of-the-Art Advances in the Structural Diversities and Catalytic Applications of Polyoxoniobate-based Materials, *Coord. Chem. Rev.*, 2021, **440**, 213966.

23 M. Nyman, Polyoxoniobate Chemistry in the 21st Century, *Dalton Trans.*, 2011, **40**, 8049–8058.

24 H. L. Wu, Z. M. Zhang, Y. G. Li, X. L. Wang and E. B. Wang, Recent Progress in Polyoxoniobates Decorated and Stabilized via Transition Metal Cations or Clusters, *CrystEngComm*, 2015, **17**, 6261–6268.

25 Y. Y. Wu, J. Dong, C. P. Liu, X. T. Jing, H. F. Liu, Y. Guo, Y. N. Chi and C. W. Hu, Reduced Polyoxomolybdate Immobilized on Reduced Graphene Oxide for Rapid Catalytic Decontamination of a Sulfur Mustard Simulant, *Dalton Trans.*, 2021, **50**, 9796–9803.

26 D. Zhang, W. Q. Zhang, Z. G. Lin, J. Dong, N. Zhen, Y. N. Chi and C. W. Hu, Mono- and Di-Sc-Substituted Keggin Polyoxometalates: Effective Lewis Acid Catalysts for Nerve Agent Simulant Hydrolysis and Mechanistic Insights, *Inorg. Chem.*, 2020, **59**, 9756–9764.

27 X. R. Sun, J. Dong, Z. Li, H. F. Liu, X. T. Jing, Y. N. Chi and C. W. Hu, Mono-Transition-Metal-Substituted Polyoxometalate Intercalated Layered Double Hydroxides for the Catalytic Decontamination of Sulfur Mustard Simulant, *Dalton Trans.*, 2019, **48**, 5285–5291.

28 X. Q. Huang, S. Liu, G. Liu, Y. W. Tao, C. R. Wang, Y. L. Zhang, Z. Li, H. W. Wang, Z. Zhou, G. D. Shen, Z. C. Xue and D. Sun, An Unprecedented 2-fold Interpenetrated Lvt Open Framework Built from Zn6 Ring Seamed Trivacant Polyoxotungstates used for

Photocatalytic Synthesis of Pyridine Derivatives, *Appl. Catal., B*, 2023, **323**, 122134.

29 G. P. Yang, K. Li and C. W. Hu, Recent Advances in Uranium-Containing Polyoxometalates, *Inorg. Chem. Front.*, 2022, **9**, 5408–5433.

30 G. P. Yang, X. L. Zhang, Y. F. Liu, D. D. Zhang, K. Li and C. W. Hu, Self-Assembly of Keggin-type U(VI)-Containing Tungstophosphates with a Sandwich Structure: An Efficient Catalyst for the Synthesis of Sulfonyl Pyrazoles, *Inorg. Chem. Front.*, 2021, **8**, 4650–4656.

31 J. Zhou, T. Yu, K. Li, K. Zeng, G. P. Yang and C. W. Hu, Two U(VI)-Containing Silicotungstates with Sandwich Structures: Lewis Acid-Base Synergistic Catalyzed Synthesis of Benzodiazepines and Pyrazoles, *Inorg. Chem.*, 2022, **61**, 3050–3057.

32 J. Dong, J. F. Hu, Y. N. Chi, Z. G. Lin, B. Zou, S. Yang, C. L. Hill and C. W. Hu, Polyoxoniobate-Polyoxovanadate Double-Anion Catalyst for Simultaneous Oxidative and Hydrolytic Decontamination of Chemical Warfare Agent Simulants, *Angew. Chem., Int. Ed.*, 2017, **56**, 4473–4477.

33 J. Dong, H. J. Lv, X. R. Sun, Y. Wang, Y. M. Ni, B. Zou, N. Zhang, A. X. Yin, Y. N. Chi and C. W. Hu, A Versatile Self-Detoxifying Material Based on Immobilized Polyoxoniobate for Decontamination of Chemical Warfare Agent Simulants, *Chem. – Eur. J.*, 2018, **24**, 19208–19215.

34 J. Dong, X. R. Sun, N. Zhen, Z. Li, D. Liu, B. Zou, Q. P. Dai, Y. N. Chi, S. L. Chen, J. M. Poblet and C. W. Hu, Oxidative Detoxification of Nerve Agent VX Simulant by Polyoxoniobate: Experimental and Theoretical Insights, *J. Catal.*, 2021, **394**, 83–93.

35 X. Q. Li, J. Dong, H. F. Liu, X. R. Sun, Y. N. Chi and C. W. Hu, Recoverable Amphiphilic Polyoxoniobates Catalyzing Oxidative and Hydrolytic Decontamination of Chemical Warfare Agent Simulants in Emulsion, *J. Hazard. Mater.*, 2018, **344**, 994–999.

36 N. Zhen, J. Dong, Z. G. Lin, X. X. Li, Y. N. Chi and C. W. Hu, Self-Assembly of Polyoxovanadate-Capped Polyoxoniobates and their Catalytic Decontamination of Sulfur Mustard Simulants, *Chem. Commun.*, 2020, **56**, 13967–13970.

37 S. Kikkawa, S. Fukuda, J. Hirayama, N. Shirai, R. Takahata, K. Suzuki, K. Yamaguchi, T. Teranishi and S. Tamazoe, Dual Functional Catalysis of $[Nb_6O_{19}]^{8-}$-Modified $Au/Al_2O_3$, *Chem. Commun.*, 2022, **58**, 9018–9021.

38 S. Hayashi, S. Yamazoe and T. Tsukuda, Base Catalytic Activity of $[Nb_{10}O_{28}]^{6-}$: Effect of Countercations, *J. Phys. Chem. C*, 2020, **124**, 10975–10980.

39 S. Hayashi, N. Sasaki, S. Yamazoe and T. Tsukuda, Superior Base Catalysis of Group 5 Hexametalates $[M_6O_{19}]^{8-}$ (M = Ta, Nb) over Group 6 Hexametalates $[M_6O_{19}]^{2-}$ (M = Mo, W), *J. Phys. Chem. C*, 2018, **122**, 29398–29404.

40 A. L. Kaledin, D. M. Driscoll, D. Troya, D. L. Collins-Wildman, C. L. Hill, J. R. Morris and D. G. Musaev, Impact of Ambient Gases on the Mechanism of $[Cs_8Nb_6O_{19}]$-Promoted Nerve-Agent Decomposition, *Chem. Sci.*, 2018, **9**, 2147–2158.

**1444** | *Inorg. Chem. Front.*, 2023, **10**, 1436–1446

This journal is © the Partner Organisations 2023

41 Y. Y. Tian, A. L. Kaledin, D. L. Collins-Wildman, V. G. Snider, D. G. Musaev, C. L. Hill and A. I. Frenkel, Polyniobate Nanothreads for Decomposition of the Nerve Agent Simulant Dimethyl Chlorophosphate, *ACS Appl. Nano Mater.*, 2021, **4**, 5649–5654.

42 M. K. Kinnan, W. R. Creasy, L. B. Fullmer, H. L. Schreuder-Gibson and M. Nyman, Nerve Agent Degradation with Polyoxoniobates, *Eur. J. Inorg. Chem.*, 2014, 2361–2367.

43 W. W. Guo, H. J. Lv, K. P. Sullivan, W. O. Gordon, A. Balboa, G. W. Wagner, D. G. Musaev, J. Bacsa and C. L. Hill, Broad-Spectrum Liquid- and Gas-Phase Decontamination of Chemical Warfare Agents by One-Dimensional Heteropolyniobates, *Angew. Chem., Int. Ed.*, 2016, **55**, 7403–7407.

44 Y. L. Wu, X. X. Li, Y. J. Qi, H. Yu, L. Jin and S. T. Zheng, {$Nb_{288}O_{768}(OH)_{48}(CO_3)_{12}$}: A Macromolecular Polyoxometalate with Niobium Atoms Close to 300, *Angew. Chem., Int. Ed.*, 2018, **57**, 8572–8576.

45 S. L. Heng, L. Li, W. W. Li, H. Y. Li, J. Y. Pang, M. Z. Zhang, Y. Bai and D. B. Dang, Enhanced Photocatalytic Hydrogen Production of the Polyoxoniobate Modified with RGO and PPy, *Nanomaterials*, 2020, **10**, 2449.

46 J. Zheng, S. H. Fan, S. Liu, G. D. Shen, W. D. Si, X. Y. Dong, X. Q. Huang, Y. L. Zhang, Q. X. Yao, Z. Li and D. Sun, In Situ Ball-Milling Gram-Scale Preparation of Polyoxoniobate-Intercalated MgAl-Layered Double Hydroxides for Selective Aldol and Michael Addition Cascade Reactions, *Inorg. Chem. Front.*, 2022, **9**, 5607–5615.

47 Q. S. Xu, T. Huang, S. L. Li, K. Li, C. L. Li, Y. N. Liu, Y. L. Wang, C. Y. Yu and Y. F. Zhou, Emulsion-Assisted Polymerization-Induced Hierarchical Self-Assembly of Giant Sea Urchin-like Aggregates on a Large Scale, *Angew. Chem., Int. Ed.*, 2018, **57**, 8043–8047.

48 F. Yue, G. Q. Gao, F. T. Li, Y. Q. Zheng and S. F. Hou, Size-Controlled Synthesis of Urchin-like Reduced Graphene Oxide Microspheres with Highly Packed Density by Emulsion-Assisted in-situ Assembly and their Supercapacitor Performance, *Carbon*, 2018, **134**, 112–122.

49 W. Liu, G. Yang, M. P. Huang, J. W. Liang, B. B. Zeng, C. Fu and H. D. Wu, Ultrarobust and Biomimetic Hierarchically Macroporous Ceramic Membrane for Oil-Water Separation Templated by Emulsion-Assisted Self-Assembly Method, *ACS Appl. Mater. Interfaces*, 2020, **12**, 35555–35562.

50 Z. Yin, D. Ma and X. H. Bao, Emulsion-Assisted Synthesis of Monodisperse Binary Metal Nanoparticles, *Chem. Commun.*, 2010, **46**, 1344–1346.

51 J. H. Xu, S. Zhao, Y. C. Ji and Y. F. Song, Deep Desulfurization by Amphiphilic Lanthanide-Containing Polyoxometalates in Ionic-Liquid Emulsion Systems under Mild Conditions, *Chem. – Eur. J.*, 2013, **19**, 709–715.

52 A. Nisar, Y. Lu, J. Zhuang and X. Wang, Polyoxometalate Nanocone Nanoreactors: Magnetic Manipulation and Enhanced Catalytic Performance, *Angew. Chem.*, 2011, **123**, 3245–3250.

53 A. Nisar, J. Zhuang and X. Wang, Construction of Amphiphilic Polyoxometalate Mesostructures as a Highly Efficient Desulfurization Catalyst, *Adv. Mater.*, 2011, **23**, 1130–1135.

54 H. L. Li, H. Sun, W. Qi, M. Xu and L. X. Wu, Onionlike Hybrid Assemblies Based on Surfactant-Encapsulated Polyoxometalates, *Angew. Chem., Int. Ed.*, 2007, **46**, 1300–1303.

55 X. Y. Chen, H. Li, P. C. Yin and T. B. Liu, Design of Polystyrene Latex Particles Covered with Polyoxometalate Clusters via Multiple Covalent Bonding, *Chem. Commun.*, 2015, **51**, 6104–6107.

56 S. Mukhopadhyay, J. Debgupta, C. Singh, A. Kar and S. K. Das, A Keggin Polyoxometalate Shows Water Oxidation Activity at Neutral pH: POM@ZIF-8, an Efficient and Robust Electrocatalyst, *Angew. Chem., Int. Ed.*, 2018, **57**, 1918–1923.

57 Z. M. Zhang, T. Zhang, C. Wang, Z. K. Lin, L. S. Long and W. B. Lin, Photosensitizing Metal-Organic Framework Enabling Visible-Light-Driven Proton Reduction by a Wells-Dawson-Type Polyoxometalate, *J. Am. Chem. Soc.*, 2015, **137**, 3197–3200.

58 Y. W. Liu, S. M. Liu, X. Y. Lai, J. Miao, D. F. He, N. Li, F. Luo, Z. Shi and S. X. Liu, Polyoxometalate-Modified Sponge-Like Graphene Oxide Monolith with High Proton-Conducting Performance, *Adv. Funct. Mater.*, 2015, **25**, 4480–4485.

59 H. M. Asif, Y. S. Zhou, L. J. Zhang, N. Shaheen, D. Yang, J. Q. Li, Y. Long, A. Iqbal and Y. Q. Li, Covalent Synthesis of Two Hybrids Composed of Dawson-Type Polyoxometalate and Porphyrin with Remarkable Third-Order Optical Nonlinearities Reflecting the Effect of Polyoxometalates, *Inorg. Chem.*, 2017, **56**, 9436–9447.

60 L. Ullah, G. Y. Zhao, J. X. Ma, M. Usman, R. Khan and N. Hedin, Pd-Promoted Heteropolyacid on Mesoporous Zirconia as a Stable and Bifunctional Catalyst for Oxidation of Thiophenes, *Fuel*, 2022, **310**, 122462.

61 K. Shehzad, M. Ahmad, J. Y. He, T. Liu, W. H. Xu and J. H. Liu, Synthesis of Ultra-Large $ZrO_2$ Nanosheets as Novel Adsorbents for Fast and Efficient Removal of As(III) from Aqueous Solutions, *J. Colloid Interface Sci.*, 2019, **533**, 588–597.

62 S. Z. Wang, S. F. Zhou, J. Huang, G. Z. Zhao and Y. Q. Liu, Attaching $ZrO_2$ Nanoparticles onto the Surface of Graphene Oxide via Electrostatic Self-Assembly for Enhanced Mechanical and Tribological Performance of Phenolic Resin Composites, *J. Mater. Sci.*, 2019, **54**, 8247–8261.

63 B. Akram, Q. C. Lu and X. Wang, Polyoxometalate-Zirconia Coassembled Microdumbbells for Efficient Capture of Iodine, *ACS Mater. Lett.*, 2020, **2**, 461–465.

64 S. M. Zhang, N. Liu, H. W. Wang, Q. C. Lu, W. X. Shi and X. Wang, Sub-Nanometer Nanobelts based on Titanium Dioxide/Zirconium Dioxide-Polyoxometalate Heterostructures, *Adv. Mater.*, 2021, **33**, 2100576.

65 B. Sudduth, D. M. Yun, J. M. Sun and Y. Wang, Facet-Dependent Selectivity of $CeO_2$ Nanoparticles in 2-Propanol Conversion, *J. Catal.*, 2021, **404**, 96–108.

66 X. T. Jing, Z. Li, B. Lu, Y. Y. Han, Y. N. Chi and C. W. Hu, Assembly of Polyoxometalate with Graphene Foam as a

This journal is © the Partner Organisations 2023

*Inorg. Chem. Front.*, 2023, **10**, 1436–1446 | **1445**

Compressible Monolithic Catalyst for Biodiesel Production, *Appl. Catal., A*, 2020, **598**, 117613.

67 D. L. Collins-Wildman, M. Kim, K. P. Sullivan, A. M. Plonka, A. I. Frenkel, D. G. Musaev and C. L. Hill, Buffer-Induced Acceleration and Inhibition in Polyoxometalate Catalyzed Organophosphorus Ester Hydrolysis, *ACS Catal.*, 2018, **8**, 7068–7076.

68 Y. L. Wu, Y. J. Wang, Y. Q. Sun, X. X. Li and S. T. Zheng, Two High-Nuclearity Isopolyoxoniobates Containing {$Nb_{54}O_{151}$}-based Helical Nanotubes for the Decomposition of Chemical Warfare Agent Simulants, *Chem. Commun.*, 2022, **58**, 3322–3325.

69 M. C. Koning, M. van Grol and T. Breijaert, Degradation of Paraoxon and the Chemical Warfare Agents VX, Tabun, and Soman by the Metal-Organic Frameworks UiO-66-$NH_2$, MOF-808, NU-1000, and PCN-777, *Inorg. Chem.*, 2017, **56**, 11804–11809.

70 S. Kim, W. B. Ying, H. Jung, S. G. Ryu, B. Lee and K. J. Lee, Zirconium Hydroxide-Coated Nanofiber Mats for Nerve Agent Decontamination, *Chem. – Asian J.*, 2017, **12**, 698–705.

71 Y. Y. Tian, A. M. Plonka, A. M. Ebrahim, R. M. Palomino, S. D. Senanayake, A. Balboa, W. O. Gordon, D. Troya, D. G. Musaev, J. R. Morris, M. B. Mitchell, D. L. Collins-Wildman, C. L. Hill and A. I. Frenke, Correlated Multimodal Approach Reveals Key Details of Nerve Agent Decomposition by Single-Site Zr-based Polyoxometalates, *J. Phys. Chem. Lett.*, 2019, **10**, 2295–2299.

**1446** | *Inorg. Chem. Front.*, 2023, **10**, 1436–1446

This journal is © the Partner Organisations 2023